

Charge-transfer-induced re-entrant ferromagnetism in twisted-bilayer-$MoTe_2$/hBN/WSe_2

Shaozheng Wang(王绍政), Xumin Chang(常旭敏), Feng Liu(刘峰), Yuchen Zheng(郑宇辰), Juncai Wu(吴俊才), Tong Zheng(郑桐), Kenji Watanabe, Takashi Taniguchi, and Shengwei Jiang(姜生伟)

Citation: Chin. Phys. B, 2026, 35 (**2**): 027101. DOI: 10.1088/1674-1056/ae1c27
http://cpb.iphy.ac.cn; http://iopscience.iop.org/cpb

What follows is a list of articles you may be interested in

Anionic electron dimensionality and monolayer ferromagnetism in Y-Co electrides

Lu Zheng(郑璐), Zimeng Lv(吕梓萌), Xiaochen Huang(黄小琛), Zhuangfei Zhang(张壮飞), Chao Fang(房超), Yuewen Zhang(张跃文), Qianqian Wang(王倩倩), Liangchao Chen(陈良超), Xiaopeng Jia(贾晓鹏), Biao Wan(万彪), and Huiyang Gou(缑慧阳)

Chin. Phys. B, 2025, 34 (**9**): 097105. DOI: 10.1088/1674-1056/adf82f

Simultaneous control of ferromagnetism and ferroelasticity by oxygen octahedral backbone stretching

Genhao Liang(梁根豪), Hui Cao(曹慧), Long Cheng(成龙), Junkun Zha(查君坤), Mingrui Bao(保明睿), Fei Ye(叶飞), Hua Zhou(周华), Aidi Zhao(赵爱迪), and Xiaofang Zhai(翟晓芳)

Chin. Phys. B, 2024, 33 (**9**): 097101. DOI: 10.1088/1674-1056/ad553c

High-temperature ferromagnetism and strong π-conjugation feature in two-dimensional manganese tetranitride

Ming Yan(闫明), Zhi-Yuan Xie(谢志远), and Miao Gao(高淼)

Chin. Phys. B, 2023, 32 (**3**): 037104. DOI: 10.1088/1674-1056/acae7b

Prediction of one-dimensional CrN nanostructure as a promising ferromagnetic half-metal

Wenyu Xiang(相文雨), Yaping Wang(王亚萍), Weixiao Ji(纪维霄), Wenjie Hou(侯文杰),Shengshi Li(李胜世), and Peiji Wang(王培吉)

Chin. Phys. B, 2023, 32 (**3**): 037103. DOI: 10.1088/1674-1056/acb200

Mottness, phase string, and high-T_c superconductivity

Jing-Yu Zhao(赵靖宇) and Zheng-Yu Weng(翁征宇)

Chin. Phys. B, 2022, 31 (**8**): 087104. DOI: 10.1088/1674-1056/ac7a14

SPECIAL TOPIC — Moiré physics in two-dimensional materials

Charge-transfer-induced re-entrant ferromagnetism in twisted-bilayer-$MoTe_2$/hBN/WSe_2

Shaozheng Wang(王绍政)[1,†], Xumin Chang(常旭敏)[1,†], Feng Liu(刘峰)[1], Yuchen Zheng(郑宇辰)[3], Juncai Wu(吴俊才)[3], Tong Zheng(郑桐)[3], Kenji Watanabe[4], Takashi Taniguchi[4], and Shengwei Jiang(姜生伟)[1,2,5,‡]

[1] *State Key Laboratory of Micro-nano Engineering Science, School of Physics and Astronomy, Shanghai Jiao Tong University, Shanghai* 200240, *China*

[2] *Key Laboratory of Artificial Structures and Quantum Control (Ministry of Education), School of Physics and Astronomy, Shanghai Jiao Tong University, Shanghai* 200240, *China*

[3] *Zhiyuan College, Shanghai Jiao Tong University, Shanghai* 200240, *China*

[4] *National Institute for Materials Science*, 1-1 *Namiki, Tsukuba* 305-0044, *Japan*

[5] *Tsung-Dao Lee Institute, Shanghai Jiao Tong University, Shanghai* 201210, *China*

(Received 17 September 2025; revised manuscript received 29 October 2025; accepted manuscript online 6 November 2025)

Ferromagnetism in moiré flat-band systems has been extensively studied in the first valence miniband of twisted $MoTe_2$, while its controlled realization at higher moiré fillings remains largely unexplored, except for very recent works reporting correlated magnetism near half filling of the second moiré band. Here, we investigate rhombohedral-stacked twisted $MoTe_2$/hBN/WSe_2 heterostructures and uncover two distinct ferromagnetic (FM) regions: one centered near $\nu_h \approx 3$ (half filling of the second moiré valence miniband) at zero displacement field, and a re-entrant FM phase that emerges for $\nu_h > 3$ only under a finite out-of-plane electric field. These FM regions are separated by a narrow filling window with a strongly suppressed magnetic circular dichroism (MCD) response. Layer-sensitive exciton spectroscopy identifies that WSe_2 is hole-doped in the re-entrant FM region, consistent with partial charge transfer from $MoTe_2$ to WSe_2. We propose that electric-field–induced layer repopulation stabilizes the re-entrant ferromagnetic phase by pinning the effective $MoTe_2$ filling near $\nu_h \approx 3$ while adding carriers to the remote WSe_2 layer. Our results demonstrate that remote-layer population control is an effective tuning knob for magnetic ordering in higher moiré minibands, extending the design space for correlated spin–valley phases in transition metal dichalcogenide heterostructures.

Keywords: moiré superlattice, ferromagnetism, magneto-optical spectroscopy

PACS: 71.35.–y, 75.70.Tj, 78.20.Ls

DOI: 10.1088/1674-1056/ae1c27 **CSTR:** 32038.14.CPB.ae1c27

1. Introduction

Moiré materials based on semiconducting transition metal dichalcogenides (TMDs) provide unprecedented opportunities to study quantum phases emerging from the interplay of band topology and strong correlations.[1–3] A prominent example is the realization of fractional quantum anomalous Hall (FQAH) states — fractional Chern insulators at zero magnetic field — in twisted $MoTe_2$ ($tMoTe_2$) and graphene-based Chern bands.[4–7] While most experimental efforts have focused on the first moiré valence flat band,[4–14] recent studies have begun to explore correlated and magnetic phenomena near half filling of the second moiré valence band in twisted $MoTe_2$,[15–17] partly due to analogies with higher Landau levels that can host even-denominator fractional quantum Hall physics.[18–24]

In this work, we perform magneto-optical (MCD) and exciton-sensing measurements on R-stacked $tMoTe_2$/hBN/WSe_2 devices. We detect a ferromagnetic phase centered near $\nu_h \approx 3$ (half filling of the second moiré band) at $E \approx 0$, and a distinct ferromagnetic region at $\nu_h > 3$ that emerges only under a finite electric field. We argue that this re-entrant high-filling ferromagnetism is consistent with an electric-field–induced charge transfer mechanism.

2. Device structure and twist angle calibration

Figure 1(a) schematically illustrates the dual-gate device structure of $tMoTe_2$/hBN/WSe_2 employed in this study. Devices were fabricated using the standard tear-and-stack and dry transfer method. We use few-layer $TaSe_2$ as contact electrodes, taking advantage of its high work function to facilitate good electrical contact for hole doping in $tMoTe_2$. Thin flakes of hexagonal boron nitride (hBN), graphite (3–5 nm), monolayer $MoTe_2$, monolayer WSe_2, and $TaSe_2$ (2–5 nm) were first exfoliated from bulk crystals onto Si/SiO_2 (285 nm) substrates. Flakes of appropriate thickness were identified according to their reflectance contrast under an optical microscope. The $MoTe_2$ monolayer was mechanically cut into two parts using atomic force microscope (AFM) tips. $MoTe_2$ flakes were

[†] These authors contributed equally to this work.

[‡] Corresponding author. E-mail: swjiang@sjtu.edu.cn

© 2026 Chinese Physical Society and IOP Publishing Ltd. All rights, including for text and data mining, AI training, and similar technologies, are reserved.

handled inside a liquid-nitrogen-filled glovebox with oxygen and water levels below 0.01 ppm to minimize degradation. The moiré $MoTe_2$ bilayer and the WSe_2 monolayer are separated by an ultrathin hBN layer with a thickness of approximately 1 nm. The complete dual-gated structure was assembled using a polycarbonate stamp. The stack was then released on the pre-patterned and cleaned Ti (5 nm)/Au (20 nm) electrodes on Si/SiO_2 substrates, such that the graphite gates and $TaSe_2$ grounding contact were electrically connected to the deposited contacts.

The dual-gated structure enables independent control of the doping density (n) and the vertical electric field (E). Here, we define $E = D/\varepsilon_0$ as the applied electric field in vacuum, where D is the displacement field and ε_0 is the vacuum permittivity. The carrier density n and E on the sample are converted from the top (bottom) gate voltage V_t (V_b) using a parallel plate capacitor model

$$n = \frac{V_t C_t + V_b C_b}{e} = \frac{1}{e}\left(\frac{\varepsilon_0 \varepsilon_t}{d_t} V_t + \frac{\varepsilon_0 \varepsilon_b}{d_b} V_b\right),$$

$$D = \frac{V_b C_b - V_t C_t}{2} - D_{\text{offset}} = \frac{1}{2}\left(\frac{\varepsilon_0 \varepsilon_b}{d_b} V_b - \frac{\varepsilon_0 \varepsilon_t}{d_t} V_t\right) - D_{\text{offset}},$$

where e is the electron charge, $\varepsilon_b = \varepsilon_t = \varepsilon_{BN}$ is the relative dielectric constant of bottom and top hBN layers, and C_t and C_b are the top and bottom gate capacitances obtained from the top and bottom hBN thickness d_t and d_b, which can be measured by atomic force microscopy. The offset electric field likely arises from structural asymmetry and can be determined from the symmetric axis of the dual-gate MCD map.

Figure 1(b) illustrates the honeycomb moiré lattice with two sublattices centered at the MX and XM (M = Mo; X = Te) stacking sites. A schematic illustration of the band structures for $tMoTe_2/hBN/WSe_2$ is shown in Fig. 1(c). In the vicinity of the K point of the Brillouin zone, the band structure of each $MoTe_2$ layer can be regarded as a single spin-polarized parabolic band. Interlayer coupling causes strong hybridization of the bands where they intersect, leading to moiré minibands. At $E = 0$, $tMoTe_2$ and WSe_2 have type-I band alignment with a valence band offset of ~ 300 meV (both conduction and valence band edges originate from $tMoTe_2$).[25] The band alignment of the sensor WSe_2 and $tMoTe_2$ valence bands ensures that the sensor remains neutral over a large range of hole doping densities. Applying an out-of-plane E-field can reduce the valence band offset, enabling conditional charge transfer.

We first performed dielectric sensing measurements on this system. Here, monolayer WSe_2 is used as a sensor. Changes in the $tMoTe_2$ compressibility modulate the dielectric environment for the WSe_2,[26] which is probed via its 2s exciton response.[27–30] The optical measurements were performed in reflection geometry using a home-built confocal optical microscope based on a closed-cycle helium cryostat

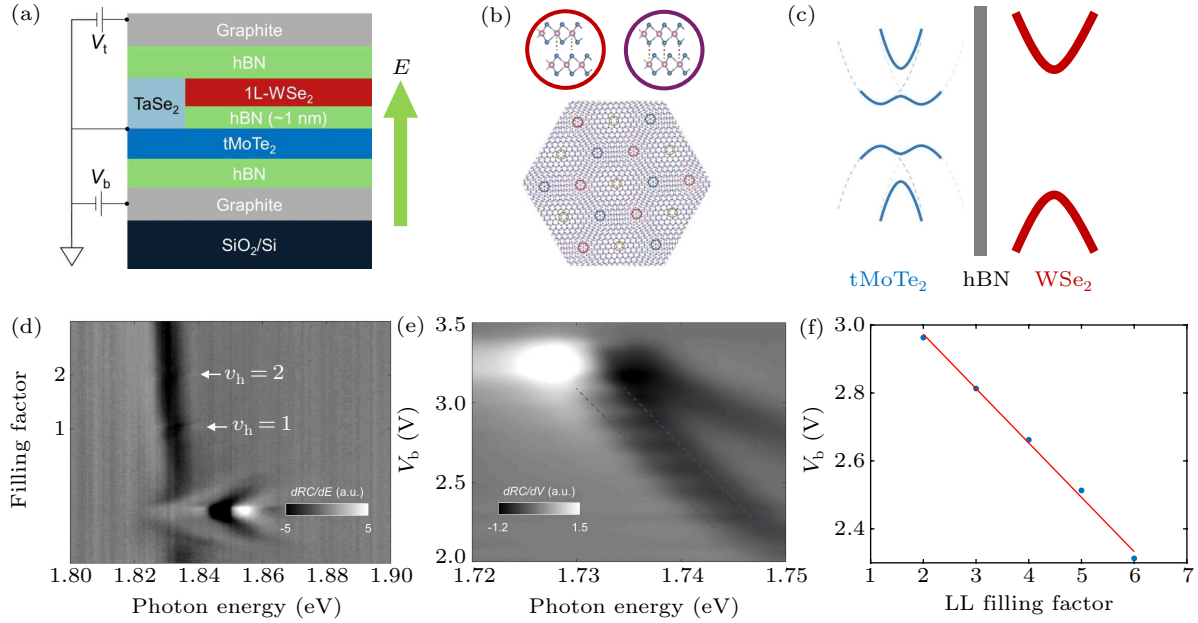


Fig. 1. (a) Schematic of a dual-gated device. V_t and V_b are the bias voltages applied to the top and bottom graphite/hBN gates, respectively. (b) The schematic moiré superlattice of R-stacked $tMoTe_2$. High-symmetry stacking sites are highlighted by circles. Red circles correspond to MX sublattice sites, where the Mo atoms in the top layer are aligned with the Te atoms in the bottom layer. Blue circles indicate the corresponding XM sublattice sites. MX and XM are two degenerate energy minima at $E = 0$, forming a honeycomb moiré superlattice. (c) Schematic representation of the band diagram of $tMoTe_2/hBN/WSe_2$ under $E = 0$. (d) ν_h-dependent differential reflection contrast spectrum showing the 2s exciton of the WSe_2 sensor, measured at $E = 0$ and $T = 1.6$ K. Arrows mark the correlated insulating states identified from the blueshift of the 2s exciton resonance. (e) Derivative polarization-resolved RC spectrum (RC_+) of the repulsive polaron with respect to V_b, dRC_+/dV_b, under 9 T at 1.6 K, with $V_t = -5.2$ V. Periodic modulations of attractive and repulsive polarons from monolayer WSe_2 reveal the formation of Landau levels (LLs). (f) V_b dependence of the LL filling factor, obtained from the minima of the integrated dRC_+/dV_b amplitude. In the V_b range shown, WSe_2 is lightly hole-doped, and the Landau levels are non-degenerate. Bottom gate capacitance $C_b/e = (1.36 \pm 0.05) \times 10^{12}$ cm$^{-2} \cdot$V^{-1} can be extracted from the linear fit denoted by the red solid line.

equipped with a superconducting magnet. For dielectric sensing, a halogen lamp is used as a white light source. Its output is first collected by a single-mode fiber and collimated by a $\times 10$ objective. The beam on the sample has a power below 10 nW, and the incident light is focused onto the device under normal incidence by a low-temperature microscope objective. The spot size of the excitation light is ~ 1 μm. Reflected light is spectrally resolved by a spectrometer coupled to a liquid-nitrogen-cooled Si charge-coupled device (CCD).

Figure 1(d) shows the 2s sensing signal of WSe_2 versus ν_h at $E = 0$. Pronounced features in the resonance-energy shift are observed at $\nu_h = 1$ and 2, signifying their incompressible nature ($\nu_h = 1$ is defined as one hole per moiré unit cell, corresponding to a half-filled moiré valence band). No evident features of fractional fillings are observed, likely due to their much smaller gap, which is beyond the sensitivity of our measurement. In principle, n can be obtained from the capacitor model and used to calculate the twist angle from the assigned filling factors. In our case, thanks to the high mobility of the device, n (and thus the twist angle) can be independently calibrated from the quantum oscillations observed optically under an out-of-plane magnetic field of 9 T. Figure 1(e) presents the doping-dependent reflectance contrast (RC) response of WSe_2 under $\sigma+$ excitation at 9 T. The oscillations result from the formation of Landau levels (LLs). Upon complete filling of the ν_{LL}th Landau level with hole carriers, the hole carrier density is expressed as $n_{LL} = \nu_{LL}|B|/\phi$, where $\phi = h/e$ (h is Planck's constant). The LL period is determined to be 0.160 ± 0.006 V for the V_b response, from which we deduce a hole density change of $(1.36 \pm 0.05) \times 10^{12}$ cm^{-2} per volt. By determining the number of filling factors corresponding to n_{LL}, the moiré density $n_M = (2.47 \pm 0.07) \times 10^{12}$ cm^{-2} is obtained. Finally, the twist angle θ is calculated to be $2.96^\circ \pm 0.04^\circ$ using $\theta = a\sqrt{\frac{\sqrt{3}}{2} n_M}$, where a is the $MoTe_2$ lattice constant, approximately 3.53 Å.

3. Observation of the re-entrant FM at $\nu_h > 3$

To investigate the filling dependence of magnetic interactions, we performed reflective magnetic circular dichroism (MCD) measurements under small B. A superluminescent light-emitting diode with a peak wavelength of 1070 nm and a full-width at half-maximum bandwidth of 90 nm was used as the light source. A combination of a linear polarizer and an achromatic quarter-wave plate generated left- and right-circularly polarized light. To avoid perturbing the system, the incident intensity on the sample was kept below 10 nW $\cdot$ μm^{-2}. Reflected light was spectrally resolved by a spectrometer coupled to a liquid-nitrogen-cooled InGaAs one-dimensional array sensor.

To analyze the MCD as a function of tuning parameters such as ν, E, B, and T, we integrate the MCD modulus over a spectral range that covers most of the MCD signal. The integrated MCD (referred to simply as the MCD below) reflects the difference in occupancy between the K and K' valleys in $MoTe_2$. Because of spin-valley locking, the signal is proportional to the out-of-plane magnetization.[31–34] In the MCD map measurements, the results are averaged over positive and negative B, i.e., $\text{MCD} = \frac{\text{MCD}(+B) - \text{MCD}(-B)}{2}$.

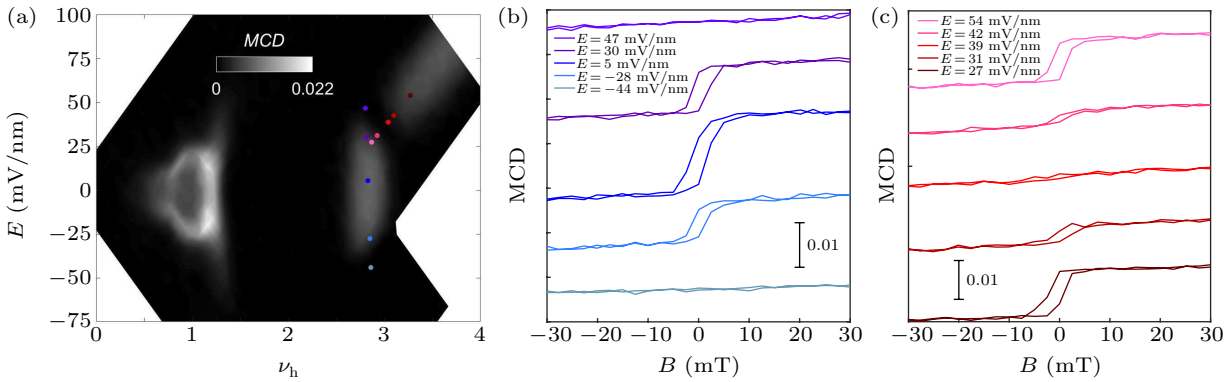


Fig. 2. (a) MCD maps as a function of ν_h and E for $tMoTe_2$/hBN/WSe_2 under a small B (10 mT). Measurements were performed at 1.6 K. (b) B dependence of MCD at representative electric fields and filling factors near $\nu_h \approx 3$. (c) B dependence of MCD at representative electric fields in the re-entrant FM region. The (ν_h, E) values corresponding to the curves are indicated by the colored dots in (a).

Figure 2(a) shows the MCD intensity plot as a function of ν_h and E, measured at 8 mT. MCD signals are observed at filling factors around both $\nu_h = 1$ and $\nu_h = 3$. In this study, we focus on the second moiré band. A clear MCD dome centered near $\nu_h = 3$ appears at low $|E|$, signifying the emergence of magnetism around the half-filling of the second moiré band. Figure 2(b) shows the MCD versus B as a function of E at $\nu_h = 3$. An appreciable hysteresis loop emerges around $E = 0$, confirming the ferromagnetic (FM) order. Applying a large E-field quenches the ferromagnetism around $\nu_h = 3$. These observations are consistent with recent studies reporting ferromagnetism around $\nu_h = 3$.[15,16]

Strikingly, at higher fillings ($\nu_h > 3$) and finite E, a second MCD-enhanced region emerges, which also exhibits magnetic

hysteresis, as shown in Fig. 2(c). The re-entrant FM region shows approximately linear ν_h–E-field dispersion, indicating that E-field–induced charge transfer may play a role.

4. Mechanism of the re-entrant FM

To uncover the origin of the re-entrant FM, we performed layer-resolved reflectance contrast (RC) measurements to identify the doping state of the WSe_2 layer. Figure 3(a) shows the RC spectra as a function of V_t. We found that the neutral exciton vanishes when V_t is sufficiently negative, signifying that the WSe_2 layer is hole-doped. Figure 3(b) shows the spectrally integrated RC as a function of ν_h and E. The bright region represents the phase space where the neutral exciton of the WSe_2 layer is strong (i.e., the WSe_2 layer is neutral). In contrast, the black region represents the phase space where the neutral exciton vanishes (i.e., the WSe_2 layer is hole-doped). At low doping density and low E-field, the WSe_2 layer is neutral, and all holes occupy the $tMoTe_2$ layer, consistent with the type-I band alignment between $tMoTe_2$ and WSe_2. However, holes are transferred from $tMoTe_2$ to WSe_2 under a sufficiently high E-field (E_c), which decreases with increasing ν_h. We found that re-entrant FM appears only in the phase space where the WSe_2 layer is hole-doped (Fig. 3(b)). Therefore, we propose that the re-entrant FM order observed at $\nu_h > 3$ is likely induced by charge transfer between $tMoTe_2$ and monolayer WSe_2.

Figure 3(c) schematically illustrates the band structures (hole-side only) for $tMoTe_2$/hBN/WSe_2 under zero and finite E-field. At $E = 0$, $tMoTe_2$ and WSe_2 have type-I band alignment with a valence band offset of ~ 300 meV. Considering that the bandwidth and energy gap of moiré minibands are on the order of tens of meV, the Fermi level (E_F) lies well above the valence band top of the WSe_2 layer, and all holes reside in the $tMoTe_2$ layer at $\nu_h \gg 3$ without an E-field (Fig. 3(c), upper panel). Consequently, $tMoTe_2$/hBN/WSe_2 behaves similarly to bare $tMoTe_2$, and FM order is absent until a finite E is applied. Applying an out-of-plane E-field reduces the valence band offset, moving the valence band top of the WSe_2 layer closer to E_F (Fig. 3(c), lower panel). Under an appropriate E-field, a certain amount of hole transfer from $tMoTe_2$ to WSe_2 occurs, keeping the effective filling factor of $tMoTe_2$ near $\nu_h \sim 3$, resulting in re-entrant FM order in the heterostructure.

The experimental observations are well captured by this scenario, except that the $\nu_h \sim 3$ and $\nu_h > 3$ regions are separated by a magnetically suppressed corridor just above $\nu_h \approx 3$ in the MCD phase diagram. This corridor cannot be understood by classical electrostatics, in which the charge transfer should vary continuously with E and ν_h, and the $\nu_h \sim 3$ and $\nu_h > 3$ regions should be connected. We believe this anomalous corridor is related to the strong correlation nature of the holes in $tMoTe_2$. One possible explanation is that when ν_h is slightly above 3, the threshold E-field for charge transfer from $tMoTe_2$ to WSe_2 is large due to correlation effects, so the $tMoTe_2$ bilayer becomes layer-polarized before charge transfer, resulting in vanishing FM order. In contrast, when ν_h is well above 3, the correlation effect is significantly suppressed by screening, resulting in a smaller E-field for charge transfer. Therefore, when charge transfer occurs, the $tMoTe_2$ remains in a layer-hybridized state, yielding re-entrant FM order. A full microscopic validation is left for future work.

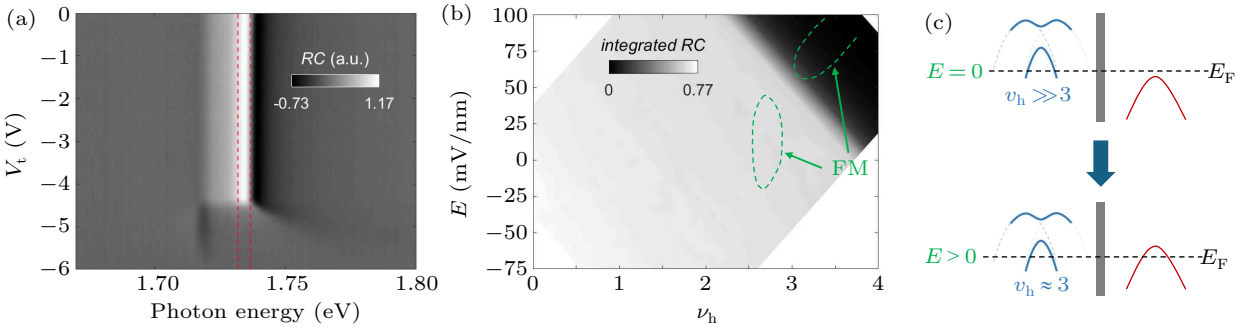


Fig. 3. (a) RC spectra as a function of V_t at V_b and $T = 1.6$ K. (b) Spectrally integrated RC as a function of ν_h and E, measured at $T = 1.6$ K. The green dashed lines indicate the boundaries of the $\nu_h \sim 3$ FM region and the re-entrant FM region. The energy range used for integration is indicated by the red dashed lines in panel (a). (c) Schematic illustration of the band structures (hole-side only) for $tMoTe_2$/hBN/WSe_2 under zero (upper panel) and finite E-field (lower panel).

5. Temperature dependence of the re-entrant FM

Finally, we study the temperature dependence of the FM order in the second moiré band. Figure 3 shows the MCD (ν_h, E) phase diagram at various temperatures. When the temperature is raised to 3 K, the high-filling ($\nu_h > 3$) FM signal weakens markedly, while the $\nu_h \approx 3$ region remains evident, indicating a lower critical temperature for the $\nu_h > 3$ region. This disparity can be understood as arising from the weakened electronic correlation and effective exchange at higher fillings in the $tMoTe_2$ layer, due to additional screening from the excess holes transferred to the nearby WSe_2 layer.

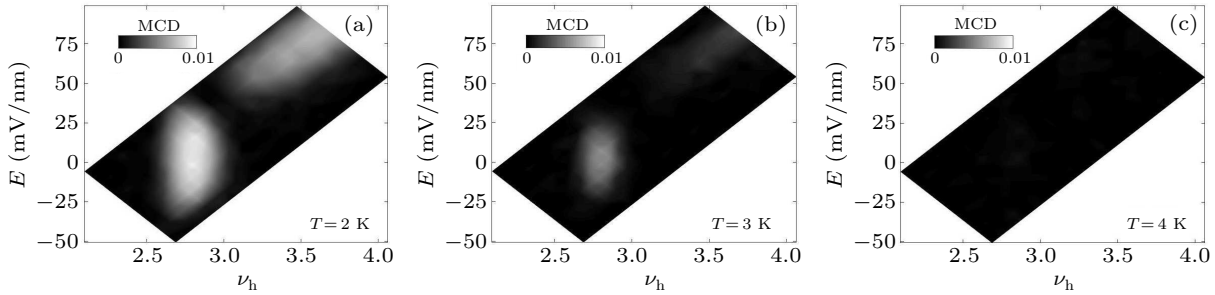


Fig. 4. (a)–(c) Evolution of the MCD maps as a function of temperature T. Each color map shows the MCD versus ν_h and E at a fixed T, under a small B (8 mT).

6. Conclusion

In summary, we observe two distinct ferromagnetic regions in twisted $MoTe_2$/hBN/WSe_2 heterostructures: a primary dome near $\nu_h \approx 3$ at low electric field, and a re-entrant high-filling FM phase ($\nu_h > 3$) that emerges only under a finite E. These regions are separated by a narrow magnetically suppressed window. Layer-sensitive exciton spectroscopy indicates that the WSe_2 layer is hole-doped in the re-entrant FM region, supporting a mechanism in which electric-field–tuned layer charge transfer promotes the re-entrant FM order. These findings establish remote-layer population control as an effective approach to engineer and reconfigure correlated magnetic phases beyond the first moiré band in TMD-based systems.

Acknowledgments

We thank Prof. Yang Zhang for fruitful discussions.

This work was supported by the National Key R&D Program of China (Grant Nos. 2021YFA1400100 and 2021YFA1401400), the National Natural Science Foundation of China (Grant Nos. 12550403, 12174250 and 12141404), and the Shanghai Jiao Tong University 2030 Initiative Program B (Grant No. WH510207202). K.W. and T.T. acknowledge support from JSPS KAKENHI (Grant Nos. 21H05233 and 23H02052) and the World Premier International Research Center Initiative (WPI), MEXT, Japan. Device fabrication was supported by the Micro-Nano Fabrication Platform of the School of Physics and Astronomy at Shanghai Jiao Tong University.

References

[1] Kennes D M, Claassen M, Xian L, Georges A, Millis A J, Hone J, Dean C R, Basov D N, Pasupathy A N and Rubio A 2021 *Nat. Phys.* **17** 155

[2] Mak K F and Shan J 2022 *Nat. Nanotechnol.* **17** 686

[3] Andrei E Y, Efetov D K, Jarillo-Herrero P, MacDonald A H, Mak K F, Senthil T, Tutuc E, Yazdani A and Young A F 2021 *Nat. Rev. Mater.* **6** 201

[4] Cai J, Anderson E, Wang C, *et al.* 2023 *Nature* **622** 63

[5] Zeng Y, Xia Z, Kang K, Zhu J, Knüppel P, Vaswani C, Watanabe K, Taniguchi T, Mak K F and Shan J 2023 *Nature* **622** 69

[6] Park H, Cai J, Anderson E, *et al.* 2023 *Nature* **622** 74

[7] Xu F, Sun Z, Jia T, Liu C, Xu C, Li C, Gu Y, Watanabe K, Taniguchi T, Tong B, Jia J, Shi Z, Jiang S, Zhang Y, Liu X and Li T 2023 *Phys. Rev. X* **13** 031037

[8] Lu Z, Han T, Yao Y, Reddy A P, Yang J, Seo J, Watanabe K, Taniguchi T, Fu L and Ju L 2024 *Nature* **626** 759

[9] Redekop E, Zhang C, Park H, *et al.* 2024 *Nature* **635** 584

[10] Ji Z, Park H, Barber M E, Hu C, Watanabe K, Taniguchi T, Chu J H, Xu X and Shen Z X 2024 *Nature* **635** 578

[11] Kang K, Shen B, Qiu Y, Zeng Y, Xia Z, Watanabe K, Taniguchi T, Shan J and Mak K F 2024 *Nature* **628** 522

[12] Xie J, Huo Z, Lu X, Feng Z, Zhang Z, Wang W, Yang Q, Watanabe K, Taniguchi T, Liu K, Song Z, Xie X C, Liu J and Lu X 2025 *Nat. Mater.* **24** 1042

[13] Choi Y, Choi Y, Valentini M, Patterson C L, Holleis L F W, Sheekey O I, Stoyanov H, Cheng X, Taniguchi T, Watanabe K and Young A F 2025 *Nature* **639** 342

[14] Lu Z, Han T, Yao Y, Hadjri Z, Yang J, Seo J, Shi L, Ye S, Watanabe K, Taniguchi T and Ju L 2025 *Nature* **637** 1090

[15] Xu F, Chang X, Xiao J, Zhang Y, Liu F, Sun Z, Mao N, Peshcherenko N, Li J, Watanabe K, Taniguchi T, Tong B, Lu L, Jia J, Qian D, Shi Z, Zhang Y, Liu X, Jiang S and Li T 2025 *Nat. Phys.* **21** 542

[16] Park H, Cai J, Anderson E, *et al.* 2025 *Nat. Phys.* **21** 549

[17] An L, Pan H, Qiu W X, *et al.* 2025 *Nat. Commun.* **16**

[18] Xu C, Mao N, Zeng T and Zhang Y 2025 *Phys. Rev. Lett.* **134** 066601

[19] Reddy A P, Paul N, Abouelkomsan A and Fu L 2024 *Phys. Rev. Lett.* **133** 166503

[20] Sodemann V I 2024 *Phys. Rev. B* **110** 045114

[21] Wang C, Zhang X W, Liu X, Wang J, Cao T and Xiao D 2025 *Phys. Rev. Lett.* **134** 076503

[22] Zhang Y H 2024 *Phys. Rev. B* **110** 155102

[23] May-Mann J, Stern A and Devakul T 2025 *Phys. Rev. B* **111** L201111

[24] Jian C M, Cheng M and Xu C 2025 *Phys. Rev. X* **15** 021063

[25] Li T, Jiang S, Shen B, Zhang Y, Li L, Tao Z, Devakul T, Watanabe K, Taniguchi T, Fu L, Shan J and Mak K F 2021 *Nature* **600** 641

[26] Raja A, Chaves A, Yu J, Arefe G, Hill H M, Rigosi A F, Berkelbach T C, Nagler P, Schüller C, Korn T, Nuckolls C, Hone J, Brus L E, Heinz T F, Reichman D R and Chernikov A 2017 *Nat. Commun.* **8**

[27] Xu Y, Liu S, Rhodes D A, Watanabe K, Taniguchi T, Hone J, Elser V, Mak K F and Shan J 2020 *Nature* **587** 214

[28] Popert A, Shimazaki Y, Kroner M, Watanabe K, Taniguchi T, Imamoglu A and Smoleński T 2022 *Nano Lett.* **22** 7363

[29] Gu J, Zhu J, Knuppel P, Watanabe K, Taniguchi T, Shan J and Mak K F 2024 *Nat. Mater.* **23** 219

[30] Zhang Z, Regan E C, Wang D, *et al.* 2022 *Nat. Phys.* **18** 1214

[31] Anderson E, Fan F R, Cai J, Holtzmann W, Taniguchi T, Watanabe K, Xiao D, Yao W and Xu X 2023 *Science* **381** 325

[32] Tang Y, Li L, Li T, Xu Y, Liu S, Barmak K, Watanabe K, Taniguchi T, MacDonald A H, Shan J and Mak K F 2020 *Nature* **579** 353

[33] Ciorciaro L, Smoleński T, Morera I, K *et al.* 2023 *Nature* **623** 509

[34] Tao Z, Zhao W, Shen B, Li T, Knüppel P, Watanabe K, Taniguchi T, Shan J and Mak K F 2024 *Nat. Phys.* **20** 783